JACS
JOURNAL OF THE AMERICAN CHEMICAL SOCIETY
Article
Cite This: J. Am. Chem. Soc. 2019, 141, 20107−20117
pubs.acs.org/JACS

Seeded Heteroepitaxial Growth of Crystallizable Collagen Triple Helices: Engineering Multifunctional Two-Dimensional Core−Shell Nanostructures

Andrea D. Merg,[†] Eric van Genderen,[‡] Alisina Bazrafshan,[†] Hanquan Su,[†] Xiaobing Zuo,[§] Gavin Touponse,[†] Thorsten B. Blum,[‡] Khalid Salaita,[†] Jan Pieter Abrahams,[‡,∥] and Vincent P. Conticello*[,†]

[†]Department of Chemistry, Emory University, Atlanta, Georgia 30322, United States
[‡]Paul Scherrer Institut, CH-5232 Villigen, Switzerland
[§]X-ray Science Division, Argonne National Laboratory, Lemont, Illinois 60439, United States
[∥]Center for Cellular Imaging and NanoAnalytics, Biozentrum, University of Basel, CH-4058 Basel, Switzerland

Supporting Information

ABSTRACT: Engineering free-standing 2D nanomaterials with compositional, spatial, and functional control across size regimes from the nano- to mesoscale represents a significant challenge. Herein, we demonstrate a straightforward strategy for the thermodynamically controlled fabrication of multicomponent sectored nanosheets in which each sector can be chemically and spatially addressed independently and orthogonally. Collagen triple helices, comprising collagen-mimetic peptides (CMPs), are employed as molecularly programmable crystallizable units. Modulating their thermodynamic stability affords the controlled synthesis of 2D core−shell nanostructures via thermally driven heteroepitaxial growth. Structural information, gathered from SAXS and cryo-TEM, reveals that the distinct peptide domains maintain their intrinsic lattice structure and illuminates various mechanisms employed by CMP triple helices to alleviate the elastic strain associated with the interfacial lattice mismatch. Finally, we demonstrate that different sectors of the sheet surface can be selectively functionalized using bioorthogonal conjugation chemistry. Altogether, we establish a robust platform for constructing multifunctional 2D nanoarchitectures in which one can systematically program their compositional, spatial, and functional properties, which is a significant step toward their deployment into functional nanoscale devices.

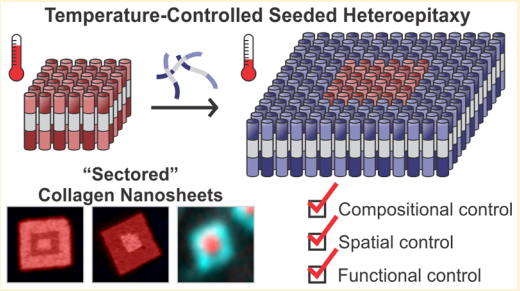

INTRODUCTION

The self-organization of macromolecular building blocks into complex, functional systems is ubiquitous in nature. These biomolecular assemblies serve as inspiration for the creation of synthetic multicomponent materials that possess similar degrees of spatial and chemical complexity. This concept provides the intellectual underpinning for the emergent field of nanoarchitectonics, in which nanomaterials with tailorable structure and properties are engineered for real-world applications.[1−3]

Free-standing two-dimensional (2D) nanomaterials represent an attractive class of synthetic targets within the nanoarchitectonic field.[4−8] The intrinsic physical properties derived from their ultrathin construction coupled with the ability to selectively functionalize the assembly surface give rise to 2D substrates that have potential utility for a diverse set of applications (e.g., biosensors, selectively permeable membranes, cell-instructive surfaces, biocatalytic and electronic scaffolds, and material components for biomedical implants/devices).[4−14] However, the vast majority of current methods involving the bottom-up fabrication of 2D nanomaterials yield heterogeneous distributions of assembled products with limited compositional, spatial, and functional control. Consequently, new synthesis protocols, in which one can systematically tailor the chemical and physical properties of 2D nanostructures, are critical for realizing their potential applications.

Recently, crystallization-driven seeded growth has been developed as a method for the controlled fabrication of 2D nanomaterials derived from organic and organometallic polymers.[15−21] Although this method affords assemblies with tailorable structure and composition, the scope of this seeded growth process is, thus far, relatively limited. Expanding the repertoire of programmable building blocks to encompass peptides and proteins, which display a rich portfolio of structure and function, would open the door for developing new classes of functional 2D biomaterials. In contrast to

Received: August 28, 2019
Published: December 4, 2019

DOI: 10.1021/jacs.9b09335
J. Am. Chem. Soc. 2019, 141, 20107−20117

synthetic polymers, peptides and proteins display precisely defined sequences, which can be configured to introduce specific, directional interactions between subunits at the nanoscale and thereby promote the formation of structurally defined assemblies. Moreover, as precisely defined polymers of biocompatible amino acids, their chemical composition bodes well for the integration of the resultant materials with biological systems.

Previously, we reported the fabrication of nanosheets derived from collagen-mimetic peptides (CMPs).[22−24] CMP sequences comprise a triblock architecture having three sequential blocks of positively, neutral, and negatively charged triads (Figure 1a). Upon folding, CMP triple helices assemble into a crystalline 2D lattice via Coulombic interactions between oppositely charged residues on structurally adjacent triple helices (Figure 1b). We have observed that for certain CMPs the outcome of this self-assembly process is the formation of structurally homogeneous nanosheets, in which the nanosheet size and thermal stability depend on the thermodynamic stability of the corresponding CMP triple helix.[24] To ensure that self-assembly occurs via a controlled process, CMP solutions are first heated to temperatures above the melting temperature (T_m) of the corresponding nanosheet to remove kinetically trapped intermediates that can result from peptide synthesis and purification. Gradual cooling of these solutions of monomeric CMPs to temperatures below the triple helix T_m initiates the slow, controlled formation of CMP triple helices, which triggers the spontaneous nucleation and growth of 2D collagen nanocrystals.

The dependence of nanosheet formation on triple helix stability presents the opportunity to control the self-assembly process through manipulation of the solution temperature.

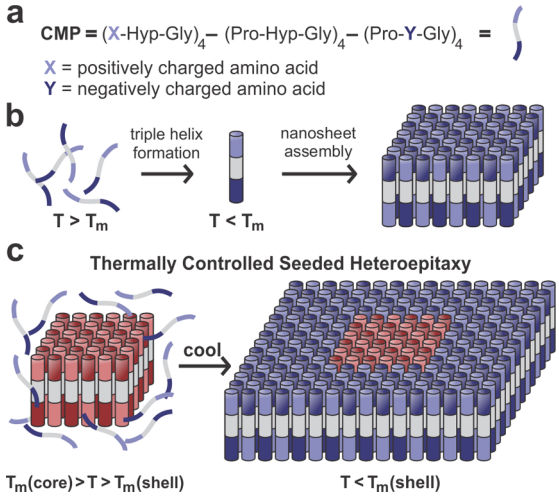

Figure 1. CMP nanosheet assembly. (a) Amino acid sequence of a CMP having triblock architecture with four neutral, positively, and negatively charged triad segments. (b) Folding of CMPs into collagen triple helices upon cooling the assembly solution below the triple helix T_m triggers their spontaneous assembly into a 2D lattice. CMP triple helices pack in an antiparallel fashion to facilitate favorable charge interactions between structurally adjacent triple helices. (c) At solution temperatures in which T_m(core) > T > T_m(shell), core nanosheet seeds (red) remain stable while shell CMPs (blue) are monomeric. Gradual cooling of the assembly solution to T < T_m(shell) should lead to the formation of sectored core−shell nanosheets.

Furthermore, we previously demonstrated that molecular engineering of the CMP sequence enables control of the triple helix T_m and the thermodynamic stability of the corresponding nanosheets.[24] These observations suggest that CMP triple helices having different T_m values can be employed to construct multicomponent core−shell nanosheets using a temperature-controlled seeded growth assembly process. Specifically, preformed nanosheets derived from CMPs displaying higher thermal stability (i.e., higher triple helix T_m values) can serve as crystalline templates for the thermally controlled heteroepitaxial growth of CMP triple helices that possess a lower melting transition. The key feature of this process is that the assembly temperature can be maintained such that T_m(core) > T > T_m(shell) (i.e., between the T_m of both core and shell CMP triple helices). Under these conditions, the shell peptide is in its monomeric form while nanosheet seeds that comprise the core persist in the self-assembled state (Figure 1c). We propose that gradually cooling the solution to below the T_m of the shell CMPs should lead to their controlled triple helix formation. The nascent triple helices can then deposit onto the lateral edges of the preexisting core nanosheets via the same Coulombic interactions that drive 2D self-assembly.

Herein, we present a versatile and straightforward strategy for the design and synthesis of multicomponent 2D assembly platforms using thermally controlled seeded growth assembly. These resultant sectored nanosheets exhibit a core−shell architecture in which each sector can be chemically and structurally addressed. The present work establishes new design and engineering principles for assembling multifunctional, 2D biomolecular nanostructures that display compositional, spatial, and functional control at the nanoscale, which is a significant development within the realm of 2D nanoarchitectonics.

RESULTS AND DISCUSSION

Independent Nanosheet Studies. Suitable CMP candidates must possess differentiable thermal stabilities, as determined from the T_m of the respective homomeric assemblies, in order to effectively perform thermally controlled heteroepitaxy. A previously studied CMP, $\mathbf{4S(X)}_{444}$, assembles into uniform nanosheets at 4 °C.[23,24] Its formation at low temperature is attributed to the presence of noncanonical (2*S*, 4*S*)-4-aminoproline (amp; Figure 2a) residues in the Xaa position, which has been shown to destabilize the collagen triple-helical structure.[25] With this in mind, we surmised that incorporating a more sterically favorable analogue, (2*S*, 4*R*)-4-aminoproline (Amp; Figure 2a), at homologous sites within the peptide sequence would yield assemblies with greater thermodynamic stability despite a similar macromolecular architecture, thereby preserving the Coulombic interactions that maintain the integrity of the 2D lattice.[25] We hypothesized that assemblies of this peptide, termed $\mathbf{4R(X)}_{444}$ (Figure 2a), could serve as seeds for the epitaxial growth of $\mathbf{4S(X)}_{444}$ triple helices.

Initial studies were conducted to independently characterize the properties of homogeneous nanosheets arising from the self-assembly of the corresponding $\mathbf{4S(X)}_{444}$ and $\mathbf{4R(X)}_{444}$ peptides. The purified CMPs (Figures S1 and S2) assemble into well-defined nanosheets in MOPS buffer (pH 7.0) under conditions in which the samples were heated to above the respective T_m values and then slowly cooled to the incubation temperature (Figure S3). In the absence of thermolysis, ill-

DOI: 10.1021/jacs.9b09335
J. Am. Chem. Soc. 2019, 141, 20107−20117

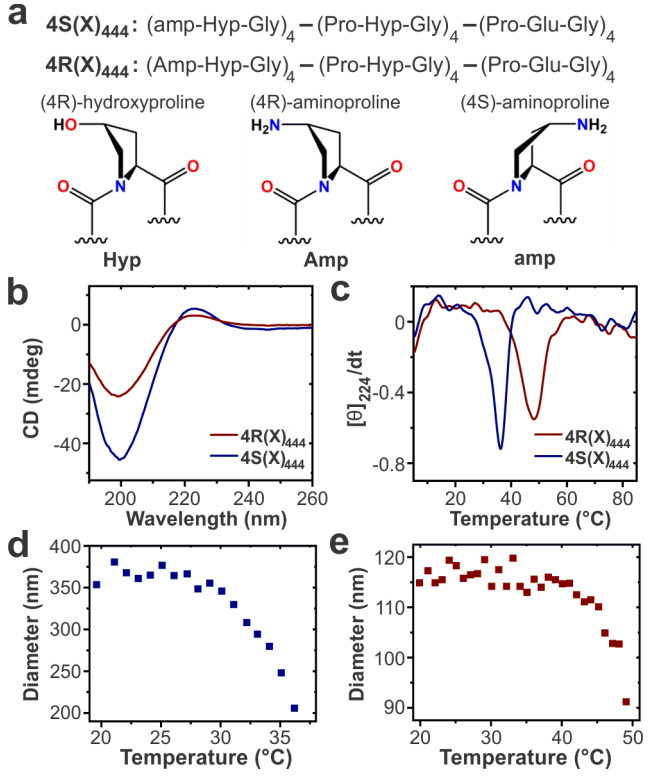

Figure 2. $\mathbf{4S(X)}_{444}$ and $\mathbf{4R(X)}_{444}$ nanosheet characterization. (a) Amino acid sequences of $\mathbf{4S(X)}_{444}$ and $\mathbf{4R(X)}_{444}$. Structures and ring pucker conformers of the incorporated imino acid derivatives are also shown. (b) CD spectra of $\mathbf{4S(X)}_{444}$ and $\mathbf{4R(X)}_{444}$ nanosheets. (c) First derivative of the CD signal at 224 nm as a function of temperature for $\mathbf{4S(X)}_{444}$ (2 mg/mL) and $\mathbf{4R(X)}_{444}$ (0.2 mg/mL) nanosheets. DLS melting curves of (d) $\mathbf{4S(X)}_{444}$ and (e) $\mathbf{4R(X)}_{444}$ nanosheets. All data were collected on nanosheets assembled after 2 weeks of incubation.

defined structures are observed, which validates the importance of thermal annealing (Figure S4). Circular dichroism (CD) spectropolarimetry of the nanosheets displays the characteristic profile of collagen triple helices, which is marked by maximum and minimum peaks at 224 and 198 nm, respectively (Figure 2b). Importantly, as predicted, CD thermal denaturation studies reveal triple-helical melting transitions at 48 and 36 °C (ΔT_m = 12 °C) for $\mathbf{4R(X)}_{444}$ (0.2 mg/mL) and $\mathbf{4S(X)}_{444}$ (2 mg/mL) nanosheets, respectively (Figure 2c). It is important to note that the T_m values pertain to triple helices *within* the 2D assembly. Previous studies have provided no evidence for the formation of isolated triple helices (i.e., in the absence of self-assembly into nanosheets).[24] The respective peptide concentrations (0.2 and 2 mg/mL for $\mathbf{4R(X)}_{444}$ and $\mathbf{4S(X)}_{444}$, respectively) reflect the optimized conditions employed in subsequent seeded growth experiments (vide infra). These conditions provide more easily distinguishable shell growth, as measured in terms of the change in nanosheet dimensions, which facilitates their characterization using microscopy techniques.

In conjunction with CD, dynamic light scattering (DLS) was employed to monitor the thermal stability and relative size distribution of the resultant nanosheets (Figure 2d,e). Although the Stokes–Einstein equation is not valid for determining absolute dimensions for 2D particles, a uniform size distribution was observed for nanosheets derived from either CMP. Therefore, DLS can provide information regarding relative changes in nanosheet size in situ. A significant decrease in particle size occurs at the respective triple helix T_m of $\mathbf{4S(X)}_{444}$ and $\mathbf{4R(X)}_{444}$ nanosheets, confirming the hypothesis that the triple helix is essential for sheet integrity. The coincidence of the melting transition observed from CD thermolysis experiments with a decrease in the DLS scattering intensity reinforces the previously observed notion that triple helix formation is a prerequisite for nanosheet self-assembly.

Core–Shell Nanosheet Assemblies. Motivated by these preliminary results, temperature-controlled seeded growth experiments were performed (Figure 3a). A dilute solution of preassembled $\mathbf{4R(X)}_{444}$ nanosheets (0.2 mg/mL) was combined with $\mathbf{4S(X)}_{444}$ (2 mg/mL). The mixture was heated and held at 40 °C for 30 min. At this temperature and concentration, $\mathbf{4R(X)}_{444}$ nanosheet seeds persist in solution (T_m = 48 °C), while $\mathbf{4S(X)}_{444}$ is monomeric (T_m = 36 °C; Figure S5). After 30 min, the solution was gradually cooled and incubated at 4 °C. Substantially larger nanosheets (diagonal length L_d = 525 ± 137 nm) are observed after 11 days of incubation (Figure 3b–d). These well-defined structures sharply contrast with identical experiments that were conducted without thermal input, which yielded polymorphic and ill-defined products (Figure S6).

To confirm that these structures comprise distinct core and shell domains, biotin–streptavidin bioconjugation was employed to probe the sheet surface. N-Terminal biotinylated derivatives of $\mathbf{4S(X)}_{444}$ and $\mathbf{4R(X)}_{444}$ were synthesized and purified (Figure S7). Because of the large size of streptavidin (~4 nm),[26] a small fraction of biotinylated peptide was deemed sufficient for the saturation of the sheet surface. Biotin-doped (5%) $\mathbf{4R(X)}_{444}$ ($\mathbf{b\text{-}4R(X)}_{444}$) assembles into nanosheets of comparable size with respect to their pure $\mathbf{4R(X)}_{444}$ counterpart (L_d = 149 ± 47 nm, Figure S8a,b). The lack of a detectable change in T_m implies that the presence of biotin has no observable effect on the triple helix stability (Figure S8c). As previously observed, seeded growth experiments yield larger sheets with dimensions similar to those of $\mathbf{4R(X)}_{444}$@$\mathbf{4S(X)}_{444}$ (core@shell) nanosheets (L_d = 562 ± 87 nm, Figure S9). Atomic force microscopy (AFM) analysis, after streptavidin addition, confirms the core–shell architecture (Figures 3f and S10).

Further analysis of the AFM data determined that diblock assemblies account for ~85% of the product distribution with the remaining ~15% representing self-nucleated $\mathbf{4S(X)}_{444}$ nanosheets, which indicates that $\mathbf{4S(X)}_{444}$ triple helices favor epitaxial growth over self-nucleation.[24] Although representing a minor product, the formation of pure $\mathbf{4S(X)}_{444}$ nanosheets highlights the importance of employing CMP triple helices that exhibit slow nanosheet nucleation kinetics. Analogous experiments, conducted on $\mathbf{4R(X)}_{444}$@$\mathbf{b\text{-}4S(X)}_{444}$ sheets, yield similar results (Figures 3g and S11 and S12). Height traces measured across the center of streptavidin-coated sheets show distinct height differences of ~4 nm, indicating the successful site-specific immobilization of streptavidin (Figure 3e–g).

Synchrotron small-angle/wide-angle X-ray scattering (SAXS/WAXS) experiments were carried out to characterize the internal structure of $\mathbf{4R(X)}_{444}$@$\mathbf{4S(X)}_{444}$ nanosheets. To discern whether the distinct peptide domains maintain their intrinsic lattice parameters, homomeric $\mathbf{4R(X)}_{444}$ and $\mathbf{4S(X)}_{444}$ nanosheets were also studied. Scattering curves of all three CMP assembly solutions verify a similar underlying structure (Figure 3h). Form-factor scattering intensities in the low-q

DOI: 10.1021/jacs.9b09335
J. Am. Chem. Soc. 2019, 141, 20107–20117

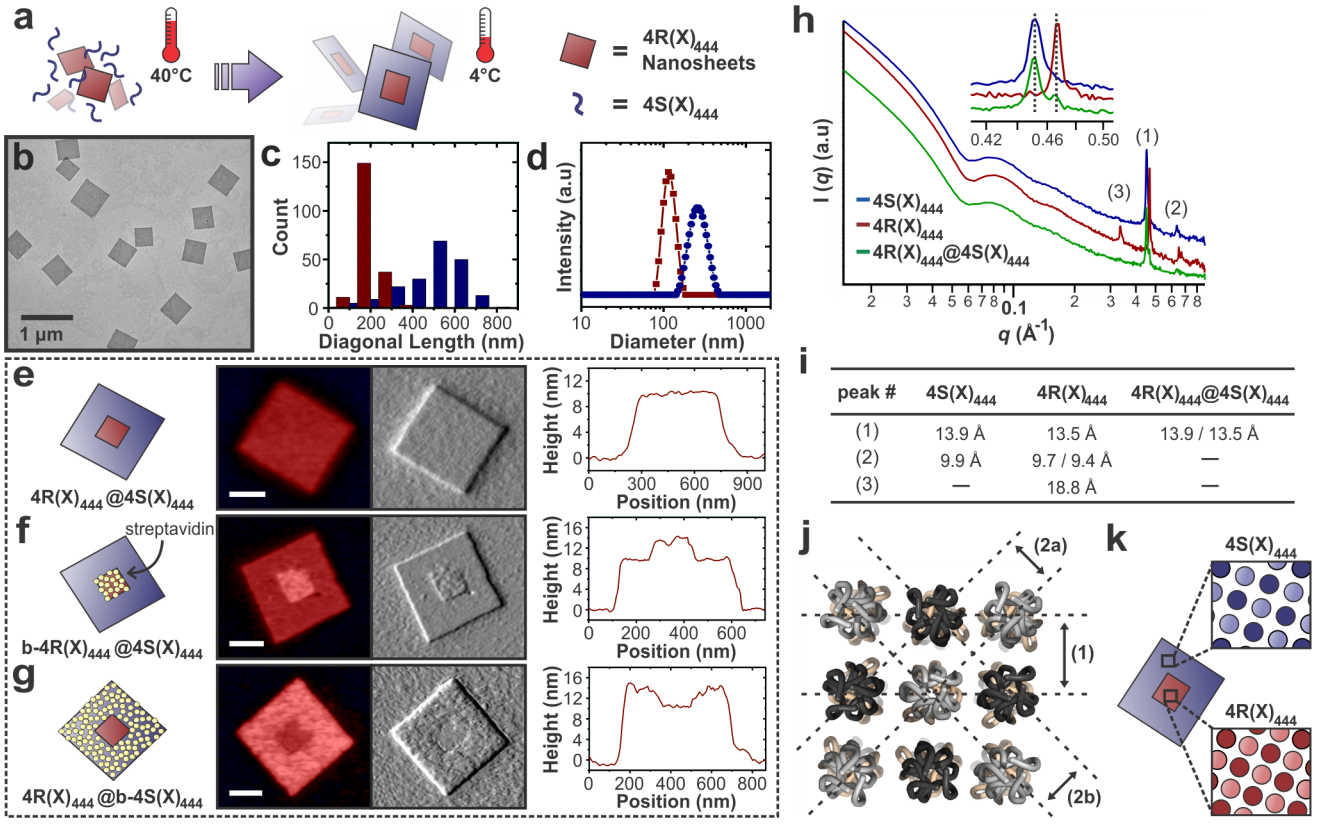

Figure 3. Core−shell nanosheet assembly and characterization. (a) Scheme detailing the assembly of $\mathbf{4R(X)_{444}@4S(X)_{444}}$ nanosheets via thermally controlled seeded growth. (b) Stained TEM image of $\mathbf{4R(X)_{444}@4S(X)_{444}}$ nanosheets after 11 days of assembly time. (c) Diagonal length distribution of $\mathbf{4R(X)_{444}}$ nanosheet seeds (red bars, 163 ± 49 nm, based on 200 counts) and $\mathbf{4R(X)_{444}@4S(X)_{444}}$ nanosheets (blue bars, 525 ± 137 nm, based on 200 counts) after 2 weeks and 11 days of assembly time, respectively. (d) DLS spectra of $\mathbf{4R(X)_{444}}$ nanosheet seeds (red line) and $\mathbf{4R(X)_{444}@4S(X)_{444}}$ nanosheets (blue line). AFM data (left to right: core−shell nanosheet model; height image (scale bar = 200 nm), amplitude image, and height profile across the center of the core−shell nanosheet) for (e) $\mathbf{4R(X)_{444}@4S(X)_{444}}$, (f) streptavidin-coated $\mathbf{b\text{-}4R(X)_{444}@4S(X)_{444}}$, and (g) streptavidin-coated $\mathbf{4R(X)_{444}@b\text{-}4S(X)_{444}}$ nanosheets. (h) Synchrotron SAXS scattering profile of $\mathbf{4S(X)_{444}}$, $\mathbf{4R(X)_{444}}$, and $\mathbf{4R(X)_{444}@4S(X)_{444}}$ nanosheets and (i) corresponding *d*-spacing values associated with peaks (1), (2), and (3). (j) Assembly packing model of collagen triple helices ordered into a 2D tetragonal lattice. Gray and black coloring highlights the antiparallel packing between adjacent triple helices. (k) Two structurally distinct lattices are present within $\mathbf{4R(X)_{444}@4S(X)_{444}}$ nanosheets.

region (q < 0.02 Å^{-1}) roughly follow a q^{-2} power law, indicating sheetlike morphology for all CMP nanosheets. Fitting the low-q data using the Guinier equation for sheetlike forms indicates similar average sheet thicknesses that are consistent with AFM and theoretical height calculations (109.6, 105.9, and 106.1 Å for $\mathbf{4R(X)_{444}}$, $\mathbf{4S(X)_{444}}$, and $\mathbf{4R(X)_{444}@4S(X)_{444}}$ nanosheets, respectively; Figures 3e and S13). The oscillations in the q range of ∼0.04−0.2 Å^{-1} stem from the thickness of the nanosheets, and its attenuation reflects the variation in sheet thickness.[23,24]

Bragg diffraction peaks in the high-q region of the intensity plot indicate a high degree of crystallinity within the 2D assemblies (Figure 3h,i). Peaks (1) and (2) constitute the triple helix packing parameters, where the former corresponds to distances between [1, 0] or [0, 1] planes (d_{helix}) and the latter corresponds to distances between [1, 1] planes (Figure 3j).[24] Calculated *d* spacings of 13.9 and 9.9 Å for peaks (1) and (2), respectively, for $\mathbf{4S(X)_{444}}$ are consistent with a tetragonal arrangement of triple helices (9.9 Å × $\sqrt{2}$ ≈ 14 Å). In contrast, the d_{helix} for $\mathbf{4R(X)_{444}}$, corresponding to peak (1), is observed at 13.5 Å, while peak (2) is split into two Bragg peaks with *d* spacings of 9.7 and 9.4 Å (Figure S14). The presence of both peaks (corresponding to 2a and 2b in Figure 3j) implies that the tetragonal lattice is slightly distorted. Moreover, a third peak, designated as peak (3), may represent a higher-order [1, 1] plane (9.4 Å × 2 = 18.8 Å) within the $\mathbf{4R(X)_{444}}$ lattice. To summarize, the $\mathbf{4R(X)_{444}}$ lattice is slightly distorted and more contracted than its $\mathbf{4S(X)_{444}}$ counterpart.

Interestingly, two peaks are observed in the SAXS scattering curve for the $\mathbf{4R(X)_{444}@4S(X)_{444}}$ nanosheets (Figure 3h inset). Their associated d_{helix} values, which correspond to the respective lattice parameters for the individual components, indicate that the core and shell domains retain their inherent packing structure (Figure 3k). This observation is not too surprising considering that the calculated lattice mismatch is approximately 3% ((13.5 Å − 13.9 Å)/13.5 Å), which is well below the benchmark limit of 15% for the successful heteroepitaxy of polymers.[16,27] The epitaxial growth of $\mathbf{4S(X)_{444}}$ onto $\mathbf{4R(X)_{444}}$ seed templates can therefore, in part, be credited to the structurally similar lattices of both components. These results differ from previous work with block copolymers in which the core lattice structure was maintained throughout the shell layer.[16]

High-Resolution Cryo-TEM Analysis. Cryogenic transmission electron microscopy (cryo-TEM) was employed to examine the heteroepitaxial interface. Because of the high throughput afforded by automated data collection, the analysis of hundreds of nanocrystals afforded a yield of 87% diblock

DOI: 10.1021/jacs.9b09335
J. Am. Chem. Soc. 2019, 141, 20107−20117

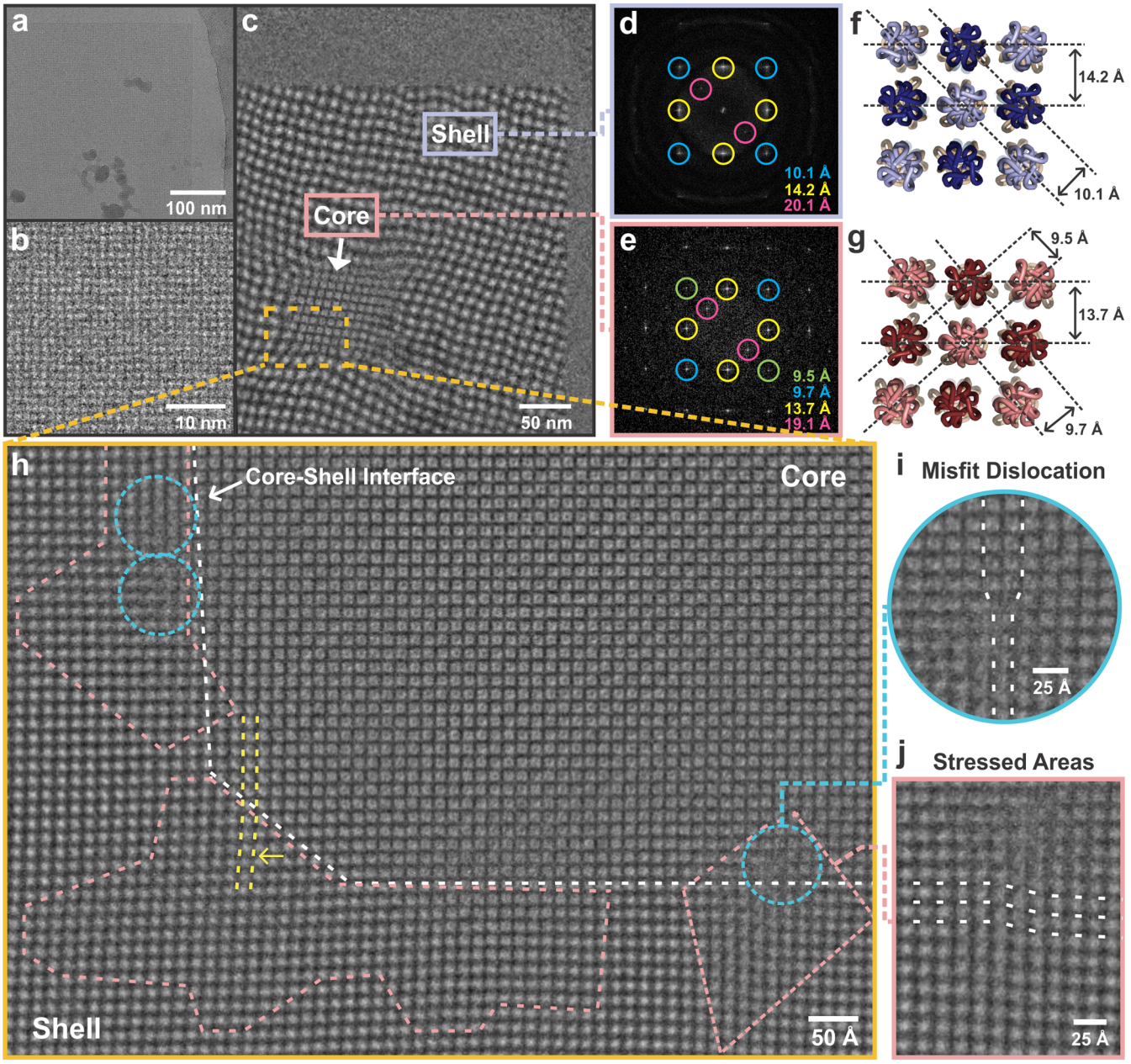

Figure 4. High-resolution cryo-TEM analysis. (a) Cryo-TEM image of a $\mathbf{4R(X)}_{444}$@$\mathbf{4S(X)}_{444}$ nanosheet. (b) Enlarged image of the $\mathbf{4R(X)}_{444}$@$\mathbf{4S(X)}_{444}$ nanosheet reveals the tetragonal arrangement of CMP triple helices comprising the 2D lattice. (c) Moiré evaluation conducted on a $\mathbf{4R(X)}_{444}$@$\mathbf{4S(X)}_{444}$ nanosheet confirms the presence of the core and shell sectors within the assembly. FFT analysis of the (d) shell and (e) core region of $\mathbf{4R(X)}_{444}$@$\mathbf{4S(X)}_{444}$ nanosheets. Proposed triple helix packing model of (f) the $\mathbf{4S(X)}_{444}$ shell and (g) the $\mathbf{4R(X)}_{444}$ core (*d* spacings obtained from FFTs). (h) Overlay of the filtered cryo-TEM image over the original drift-corrected image showing the core−shell interface (white dashed line) and the various mechanisms employed by the nanocrystal to alleviate strain associated with the interfacial lattice mismatch. Dashed blue circles indicate misfit dislocation sites, and dashed pink boxes indicate stressed areas as defined by the bending of the triple-helical rows (e.g., yellow dashed lines; arrow indicates the bending direction) and areas where the triple helices are less resolved. Enlarged image of (i) a misfit dislocation site and (j) a stressed area.

assemblies and 13% single-block assemblies (n = 463), which agree with the results acquired from AFM analysis (Figure S15). High-resolution images of $\mathbf{4R(X)}_{444}$@$\mathbf{4S(X)}_{444}$ reveal the ordered organization of individual triple-helical protomers within the 2D lattice (Figure 4a,b). To visualize the core and shell sectors, a Moiré evaluation was used in which a fixed raster was applied over the image while decreasing the image size (i.e., under sampling). At a given image scaling, the raster creates Moiré patterns, which provides visual evidence of the two sectors (Figure 4c).[28]

Fast Fourier transforms (FFTs) of cryo-TEM micrographs confirm the presence of two unique tetragonal lattices as evidenced by two distinct sets of Bragg spots that exhibit 4-fold rotational symmetry (Figure S16). Selected area FFTs of the shell and core regions were analyzed to determine the lattice packing parameters (Figure 4d,e). Sharp Bragg spots, associated with *d* spacings within the $\mathbf{4R(X)}_{444}$ lattice, extend to a resolution of ∼3.8 Å, indicating a highly ordered core (Figure S17). FFTs of the $\mathbf{4S(X)}_{444}$ shell yields less well-defined Bragg spots with corresponding *d* spacings limited to

DOI: 10.1021/jacs.9b09335
J. Am. Chem. Soc. 2019, 141, 20107−20117

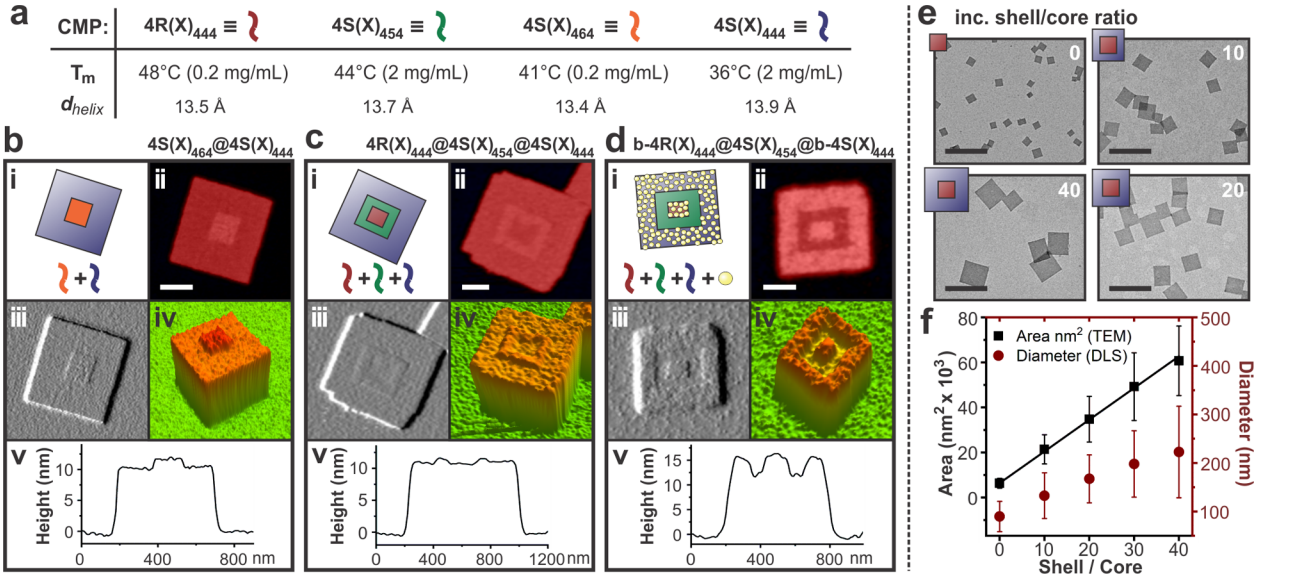

Figure 5. Compositional and size control of sectored nanosheets. (a) Various CMPs employed for assembling diblock and triblock nanosheet architectures with corresponding T_m and d_{helix} values obtained from SAXS (d_{helix} values for $\mathbf{4S(X)}_{454}$ and $\mathbf{4S(X)}_{464}$ were obtained from ref 24). AFM data [(i) nanosheet assembly model, (ii) height image, (iii) amplitude image, (iv) 3D reconstruction, and (v) height profile across the nanosheet center] of (b) $\mathbf{4S(X)}_{464}$@$\mathbf{4S(X)}_{444}$, (c) $\mathbf{4R(X)}_{444}$@$\mathbf{4S(X)}_{454}$@$\mathbf{4S(X)}_{444}$, and (d) **b-**$\mathbf{4R(X)}_{444}$@$\mathbf{4S(X)}_{454}$@**b-**$\mathbf{4S(X)}_{444}$ nanosheets (scale bars = 200 nm). (e) Stained TEM images of $\mathbf{4R(X)}_{444}$@$\mathbf{4S(X)}_{444}$ nanosheets assembled under basic conditions (pH 8.0) at various shell/core ratios (scale bars = 500 nm). (f) Linear dependence of the nanosheet area, calculated from TEM images (black line), and corresponding hydrodynamic average diameters, obtained from DLS, as a function of the shell/core ratio (error bars represent a single standard deviation).

~6.4 Å, implying that the $\mathbf{4S(X)}_{444}$ triple-helical framework is less ordered (Figure S18). Measured *d* spacings of the shell (14.2 and 10.1 Å) and core (13.7, 9.7, 9.5, and 19.1 Å) agree with values obtained from SAXS and define the *d* spacings within the triple helix packing models (Figure 4f,g).

Heteroepitaxial growth often introduces crystalline defects that arise from the necessity to alleviate elastic strain associated with the lattice mismatch.[29,30] Although this phenomenon has been studied extensively for inorganic- and polymer-based systems, heteroepitaxial interfaces within crystalline biological materials have not been fully characterized. We therefore conducted a detailed analysis of the core−shell interface, which revealed several structural distortions within the triple helix packing (Figure 4h). First, misfit dislocations are observed at sites along the core−shell border (Figure 4i). Such defects are common at the heteroepitaxial boundary arising from differences in lattice parameters between the substrate (core) and growth (shell) layers.

In addition to dislocations, the presence of stressed areas is commonly observed, which correspond to visually distinguishable areas in which triple helices are less well-resolved and in which triple helix packing is angularly distorted (e.g., bending of triple-helical rows; Figure 4h,j). We hypothesize that these stressed regions develop as a compensation mechanism in which elastic strain stemming from lattice mismatch at the core−shell interface locally overcomes the electrostatic interactions that determine the symmetry of triple helix packing. This interfacial compliance may be attributable to the deformable nature of $\mathbf{4S(X)}_{444}$ triple helices and the relatively weak cohesive interactions between them, both of which may account for a lattice that can be more easily distorted to accommodate lattice strain.[31]

The various degrees of strain within the shell sector are visualized by FFTs collected in multiple regions within the crystal. FFTs collected at positions proximal to the core reveal a greater degree of disorder (as defined by a lack of sharpness of Bragg spots) compared to FFTs collected at positions near the sheet periphery, signifying that the $\mathbf{4S(X)}_{444}$ lattice near the heteroepitaxial interface is subjected to a greater amount of strain (Figure S19). Finally, FFT analysis reveals a slight discrepancy between the orientation of the core and shell lattice (up to ~1.2°), which suggests that the $\mathbf{4S(X)}_{444}$ assembly lattice self-configures, presumably to improve alignment with the core lattice template (Figure S20).

In conclusion, these results demonstrate that the less thermodynamically stable $\mathbf{4S(X)}_{444}$ triple helices are tasked with absorbing the interfacial strain created at the heteroepitaxial interface. The apparent malleability of the softer $\mathbf{4S(X)}_{444}$ triple helix lattice, as determined by the significant presence of stressed areas, contrasts with that of rigid lattice materials (e.g., ionic solids and metals) which comprise atoms that behave as "hard spheres".[31] It is important to note that although the collagen-based structures are relatively pliable, dislocations are still required to relieve elastic strain at the core−shell interface, akin to traditional inorganic materials. These findings afford a new level of understanding of the mechanisms that underlie the heteroepitaxial growth of soft, biological structural units. We envision that these foundational insights will serve as a starting point for engineering multicomponent, multidomain assemblies from crystallizable biomolecules.

Compositional and Size Control. We hypothesized that a diverse collection of sectored nanosheets could be constructed if a wider range of CMPs were identified that met a specific set of structural criteria. We posit that the individual components should exhibit (1) a sufficient difference in thermodynamic stability (ΔT_m); (2) a comparable degree of cohesive electrostatic interactions between oppositely charged blocks; and (3) similar lattice packing parameters. Although initial studies focused on alterations to

DOI: 10.1021/jacs.9b09335
J. Am. Chem. Soc. 2019, 141, 20107−20117

the amino acid sequence (amp vs Amp) to establish an effective ΔT_m, a reasonable alternative approach would be to vary the CMP length. Increasing the number of Pro-Hyp-Gly triads has been demonstrated to increase the thermodynamic stability of collagen triple helices and their assembled structures.[24,32] Although this may decrease the number of electrostatic interactions at the core−shell interface, we anticipated that if a sufficient number of interactions are maintained, this perturbation would have a minimal effect on their coassembly.

To test this hypothesis, we employed nanosheets derived from $\mathbf{4S(X)}_{464}$,[24] which comprise two additional Pro-Hyp-Gly triads within the central block, to serve as seeds for the templated growth of $\mathbf{4S(X)}_{444}$. $\mathbf{4S(X)}_{464}$ assembles into small nanosheets with a T_m of 41 °C (0.2 mg/mL; Figures S21 and S22). Upon addition of $\mathbf{4S(X)}_{444}$, larger nanosheets are observed after 2 weeks (Figure S21). AFM analysis of $\mathbf{4S(X)}_{464}$@$\mathbf{4S(X)}_{444}$ nanosheets reveals a greater height for the central core of the resultant assemblies (Figures 5b and S23). A height difference of ∼1 nm across the center of the nanosheet is consistent with the approximate length of a single Pro-Hyp-Gly triad (0.286 nm rise/residue).[33,34] We propose that longer $\mathbf{4S(X)}_{464}$ triple helices protrude from both faces of the nanosheet, as would be expected for antiparallel triple helix packing (Figure 5b).[35]

This seeded growth process should be relatively straightforward to extend to triple-sector assemblies if three triple-helical protomers could be identified that possess significant T_m differences in the order T_m(core) > T_m(shell$_1$) > T_m(shell$_2$) (Figure 5a). Initial attempts to construct $\mathbf{4R(X)}_{444}$@$\mathbf{4S(X)}_{464}$@$\mathbf{4S(X)}_{444}$ nanosheets were unsuccessful because of the competitive self-nucleation of $\mathbf{4S(X)}_{464}$, highlighting again the importance of selecting CMPs in which self-nucleation is slower than epitaxial growth. Subsequent attempts employing $\mathbf{4S(X)}_{454}$ (2 mg/mL, T_m = 44 °C; Figure S24) as the middle layer proved to be more successful. AFM images of $\mathbf{4R(X)}_{444}$@$\mathbf{4S(X)}_{454}$ diblock assemblies reveal heteroepitaxial growth with few self-nucleated $\mathbf{4S(X)}_{454}$ nanosheets (Figure S25). $\mathbf{4S(X)}_{444}$ was introduced into a solution containing these diblock structures, and the solution was heated to 38 °C (in between the T_m of $\mathbf{4S(X)}_{454}$ and $\mathbf{4S(X)}_{444}$ triple helices) and then gradually cooled to 4 °C. An AFM analysis of the resultant $\mathbf{4R(X)}_{444}$@$\mathbf{4S(X)}_{454}$@$\mathbf{4S(X)}_{444}$ nanosheets resolved the triblock assembly architecture (Figures 5c and S26). A biotinylated derivative of the sectored triblock assembly (**b**-$\mathbf{4R(X)}_{444}$@$\mathbf{4S(X)}_{454}$@**b**-$\mathbf{4S(X)}_{444}$) was also synthesized, in which the core and outermost sectors were functionalized. The site-specific deposition of streptavidin onto the nanosheets generates a square bull's-eye pattern, which demonstrates the selective labeling of the sheet surface afforded by compositionally tuning each sector (Figures 5d and S27).

Seeded growth methods permit rational control over assembly dimensions because they minimizes the lag phase that can result in competitive self-nucleation.[15,19,36,37] The large-scale production of nanosheets with specific uniform sizes is important for bringing these 2D materials from the benchtop to the marketplace.[38] However, uniform core−shell architectures require the availability of uniform populations of seeds that can serve as templates. Through systematic studies, we determined that $\mathbf{4R(X)}_{444}$ assembles into small, monodisperse nanosheets (L_d = 106 ± 19 nm) under slightly basic conditions (pH 8.0; Figure S28). We speculate that electrostatic interactions between triple-helical protomers are weakened at higher pH, which limits the lateral growth of the resultant nanosheets. The triple helices are slightly destabilized (T_m = 42 °C, 0.2 mg/mL; Figure S29) compared to sheets grown at neutral pH. With seeds in hand, a systematic adjustment of the amount of shell peptide to core peptide ("shell/core ratio") tunes the nanosheet size across the mesoscale regime with an apparently linear dependence (Figures 5e,f and S30 and S31). We note that in the absence of seeds, $\mathbf{4S(X)}_{444}$ still forms nanosheets under basic conditions (T_m = 30 °C, 2 mg/mL) but exhibits no linear size dependence (Figure S32).

Surface Functionalization. Multiple peptide sectors within a single nanosheet offer the potential for fabricating multifunctional 2D platforms in which each sector can be individually addressed through selective chemical modification. As a proof-of-concept, a dual-binding assembly platform was constructed in which N-terminal-modified biotin and azide CMP derivatives ($\mathbf{N_3\text{-}4R(X)}_{444}$, Figure S33) were incorporated into the core and shell sectors, respectively. To visualize the site-specific binding on the sheet surface, Cy3B and AF647 fluorophores were employed as probes (Figure 6a). We note that larger, more polydisperse $\mathbf{4R(X)}_{444}$ seeds (nanosheets grown at 2 mg/mL) were used to allow for improved

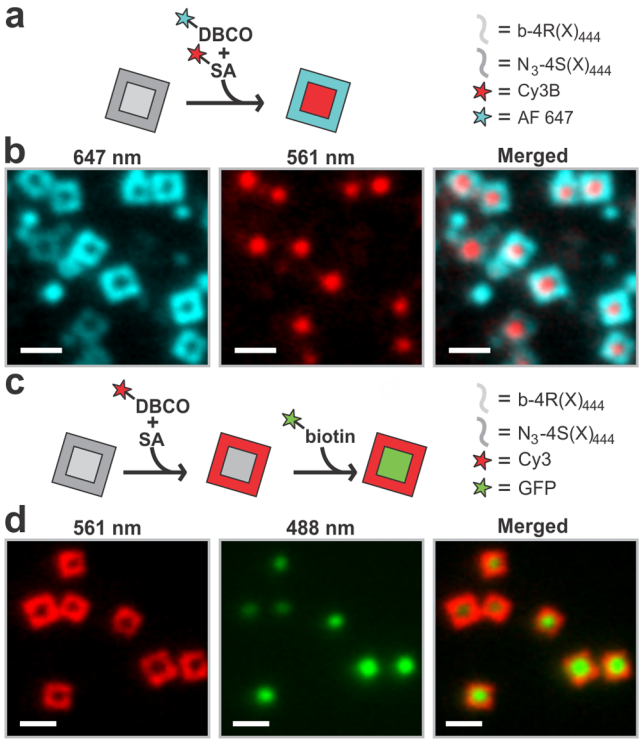

Figure 6. Surface functionalization. (a) Scheme detailing the site-specific attachment of DBCO-AF647 and SA-Cy3B onto **b**-$\mathbf{4R(X)}_{444}$@$\mathbf{N_3\text{-}4S(X)}_{444}$ nanosheets (SA = streptavidin). (b) Fluorescence optical micrographs of **b**-$\mathbf{4R(X)}_{444}$@$\mathbf{N_3\text{-}4S(X)}_{444}$ nanosheets functionalized with AF647 and Cy3B at various emission wavelengths. The observed fluorescence emissions recapitulate the core−shell assembly architecture (scale bar = 2 μm). (c) Scheme detailing the two-step site-specific attachment of DBCO-Cy3 and biotin-GFP onto **b**-$\mathbf{4R(X)}_{444}$@$\mathbf{N_3\text{-}4S(X)}_{444}$ nanosheets. (d) Fluorescence optical micrographs of **b**-$\mathbf{4R(X)}_{444}$@$\mathbf{N_3\text{-}4S(X)}_{444}$ nanosheets functionalized with Cy3 and GFP at various emission wavelengths (scale bar = 2 μm). False color was used for AF647 fluorescence to enhance the contrast.

DOI: 10.1021/jacs.9b09335
J. Am. Chem. Soc. 2019, 141, 20107−20117

visualization using fluorescence optical microscopy (Figure S34a).

A solution of **b-4R(X)$_{444}$@N$_3$−4S(X)$_{444}$** nanosheets prepared via conventional seeded growth (Figure S34b) was incubated overnight at 4 °C with streptavidin-tagged Cy3B and DBCO-tagged AF647 (DBCO = dibenzocyclooctyne). After the removal of excess dye, fluorescence optical microscopy experiments confirm the successful dual-functionalization of **b-4R(X)$_{444}$@N$_3$- 4S(X)$_{444}$** nanosheets. Cy3B fluorescent emission localizes within the core, while the AF647 fluorescence appears in the shell (Figure 6b).

Motivated by the robust, interchangeable platform accessible using bioorthogonal conjugation methods, a two-step protocol was employed to immobilize biotinylated green fluorescent protein (GFP) and Cy3 to the nanosheet core and shell, respectively (Figure 6c). Fluorescence optical micrographs confirm that the respective molecular labels segregate to the sector that is functionalized with the complementary chemical tag (Figure 6d). These results exemplify the potential use of these architecturally defined nanostructures for patterning biologically/chemically relevant cargo onto a 2D scaffold with nanoscale spatial specificity.

CONCLUSION

We present a general methodology for designing and constructing structurally and chemically tailorable 2D crystalline nanostructures, which comprise rationally engineered CMP sectors that coassemble via temperature-controlled heteroepitaxy. These nanosheets are composed of distinct CMPs that can be selectively functionalized within definable spatial regions on the nanosheet surface using bioorthogonal and biocompatible affinity binding or covalent capture. Furthermore, cryo-TEM bestows an unprecedented degree of insight into heteroepitaxial growth processes within the context of biological soft materials. The observed lattice dislocations and distortions are a consequence of the core−shell structures we describe, in view of the incompatible lattice parameters of the core and shell domains. These imperfections confirm a malleability of ordered soft matter, which is not encountered commonly in other systems. These lattice defects may allow an alternative type of specific functionalization of the core−shell structures at the defect sites (e.g., by introducing alternative components that stabilize the lattice by binding to or inserting into its defects). The present work represents an advancement in developing 2D nanomaterials with nano- to mesoscale structural and functional control via bottom-up solution-phase assembly methods.

EXPERIMENTAL METHODS

Materials and Methods. Chemical reagents were purchased from Sigma-Aldrich Chemical Co. (St. Louis, MO) and used without further purification. Fmoc-Gly-HMP-TentaGel resins were purchased from Anaspec (Fremont, CA). Boc-(2*S*, 4*S*)-4-amino-1-Fmoc-pyrrolidine-2-carboxylic acid and Boc-(2*S*, 4*R*)-4-amino-1-Fmoc-pyrrolidine-2-carboxylic acid were purchased from Chemimpex (Wood Dale, IL). Biotin-PEG2-acid and azido-PEG5-acid were purchased from Broadpharm (San Diego, CA). DBCO-Cy3 and DBCO-AF647 were purchased from Click Chemistry Tools (Scottsdale, AZ). Biotin-GFP was purchased from ProteinMods (Madison, WI). Peptides were quantified by mass and dissolved in water, followed by separation into aliquots of known amounts of peptides and lyophilization. Matrix-assisted laser desorption ionization time-of-flight mass spectrometry (MALDI-TOF) data were collected using an Applied Biosystem 4700 mass spectrometer (positive reflector mode; accelerating voltage 20 kV) and using α-cyano-4-hydroxycinnamic acid (CHCA) as the ionization matrix. Diagonal lengths of nanosheets were measured using *ImageJ*.

Peptide Synthesis and Purification. Peptides were prepared using microwave-assisted synthesis on a CEM Liberty solid-phase peptide synthesizer and Fmoc-Gly-HMP-Tentagel resin. Standard Fmoc protection chemistry was employed with coupling cycles based on HBTU/DIEA-mediated activation protocols and base-induced deprotection (20% piperidine in DMF) of the Fmoc group. For biotinylated and azide-modified peptides, biotin-PEG2-acid and azido-PEG5-acid were used to cap the N-terminus of the peptide while the peptide was still attached to the resin (no final deprotection step). After coupling, the DMF/resin mixture was filtered and rinsed with acetone and then air-dried. The crude peptides were cleaved for 3 h with a cleavage solution consisting of 92.5% TFA/2.5% H_2O/2.5% DODT/2.5% TIS (TFA = trifluoroacetic acid, DODT = 3,6-dioxa-1,8-octane-dithiol, TIS = triisopropylsilane). After filtration, the crude peptide product in TFA was precipitated with cold Et_2O and centrifuged at 4 °C. The supernatants were discarded, and the pellets were dried under vacuum overnight.

Crude peptides were purified using a Shimadzu LC-20AP reverse-phase high-performance liquid chromatography (HPLC) instrument equipped with a preparative scale C18 column. Peptides were eluted with a linear gradient of water−acetonitrile with 0.1% trifluoroacetic acid (TFA). The target fractions were collected and lyophilized. The lyophilized peptide was repurified via HPLC under the same protocol described above and lyophilized. Doubly pure peptides were dialyzed against HPLC-grade H_2O to remove residual TFA (MWCO = 2000 Da). The resulting peptide solutions were lyophilized once more and stored at −30 °C.

Sectored Nanosheet Assembly Experiments. Annealing experiments were conducted using a Fisher T-100 thermal cycler. Single-component nanosheets were dissolved in 20 mM 3-(*N*-morpholino)propanesulfonic acid (MOPS) buffer (pH 7.0) or *N*-[tris(hydroxymethyl)methyl]-3-aminopropanesulfonic acid (TAPS) buffer (pH 8.0) and held at 90 °C for 15 min and then cooled to 25 or 4 °C (0.5 °C/2.5 min rate). The sheets were allowed to assemble for 2 weeks.

Heteroepitaxial growth experiments were conducted by adding a solution of preformed nanosheet seeds (in either 20 mM MOPS buffer, pH 7.0, or 20 mM TAPS buffer, pH 8.0) to lyophilized shell peptide. The final CMP concentrations of both components were ensured by diluting a 1 mg/mL stock solution of nanosheet seeds and varying the amount of lyophilized shell peptide added to the seed solution. The peptide mixture was then held at temperatures between the T_m values of both CMPs for 30 min, except when constructing **4R(X)$_{444}$@4S(X)$_{454}$** nanosheets (hold time = 3 min). The holding temperatures varied depending on the CMPs employed: **4R(X)$_{444}$@4S(X)$_{444}$** = 40 °C; **4S(X)$_{464}$@4S(X)$_{444}$** = 37 °C; **4R(X)$_{444}$@4S(X)$_{454}$** = 44 °C; and **4R(X)$_{444}$@4S(X)$_{454}$@4S(X)$_{444}$** = 38 °C. After the hold time was completed, the solutions were cooled (0.5 °C/2.5 min) to room temperature (**4R(X)$_{444}$@4S(X)$_{454}$**) or 4 °C (**4R(X)$_{444}$@4S(X)$_{444}$**, **4S(X)$_{464}$@4S(X)$_{444}$**, and **4R(X)$_{444}$@4S(X)$_{454}$@4S(X)$_{444}$**).

Dual-Functionalization Experiments. For the AF647/Cy3B system, DBCO-AF647 (1.5 μL, 1 mg/mL solution in water) and SA-Cy3B (2 μL, 1 mg/mL solution in water) were added to a 35 μL solution of **b-4R(X)$_{444}$@N$_3$−4S(X)$_{444}$** nanosheets (2.2 mg/mL). The mixture was incubated for 1 h at room temperature in the dark and then placed in the refrigerator overnight (4 °C). The next day, the solution was centrifuged at 3500*g* for 10 min. The supernatant was removed and replaced with fresh 20 mM MOPS buffer (pH 7.0), and the sample was vortex mixed.

For the GFP/Cy3 system, DBCO-Cy3 (0.5 μL, 1 mg/mL solution in water) and streptavidin solution (1 μL, 1 mg/mL solution in water) were added to 15 μL of a solution of **b-4R(X)$_{444}$@N$_3$-4S(X)$_{444}$** nanosheets (2.2 mg/mL). The mixture was incubated for 1 h at room temperature in the dark. After 1 h, biotin-GFP (1 μL, 1.5 mg/mL) was added to the assembly solution. The solution was then placed in the refrigerator overnight. The next day, the solution was centrifuged at 3000*g* for 10 min. The supernatant was removed and replaced with

DOI: 10.1021/jacs.9b09335
J. Am. Chem. Soc. 2019, 141, 20107−20117

fresh 20 mM MOPS buffer (pH 7.0), and the sample was vortex mixed.

Circular Dichroism Spectroscopy. CD measurements were conducted on a Jasco J-810 CD spectrometer. Three spectra were recorded and averaged from 260 to 190 nm at a scanning rate of 100 nm/min and a bandwidth of 2 nm. CD melting experiments were performed in the temperature range from 5 to 85 °C at a heating rate of 20 °C/h. The intensity of the CD signal at 224 nm was monitored as a function of temperature.

Transmission Electron Microscopy. TEM images were collected with a Hitachi H-7700 transmission electron microscope at an accelerating voltage of 80 kV. TEM specimens were prepared by briefly mixing 2.5 μL of peptide nanosheet solution with 2.5 μL of aqueous uranyl acetate stain solution (1%) directly on a 200-mesh carbon-coated copper grid. After 30 s, the excess liquid was wicked away and the grids were air-dried.

Dynamic Light Scattering. DLS data were collected with a NanoPlus DLS nano particle size analyzer instrument (Particulate Systems, Norcross, GA). Three DLS measurements were obtained and averaged on aqueous solutions of CMP nanosheets at 20 °C. DLS melting experiments were conducted with a 1 cm path length cuvette at a heating rate of approximately 1 °C/3 min with a 50 s equilibration time at each degree.

Atomic Force Microscopy. AFM images were collected with an Asylum MFP-3D atomic force microscope using tapping mode. Images were obtained using ultrasharp AFM tips with a force constant of 5 N/m and a resonance frequency of 150 kHz (Budget Sensors, SHR-150). Images were collected at a scanning rate of 1 Hz. Samples were prepared by drop-casting 20 μL of peptide nanosheet solution onto freshly cleaved mica. After 5 min, the solution was wicked away and washed once with 30 μL of HPLC-grade H_2O.

Small-Angle/Wide-Angle X-ray Scattering Measurements. Synchrotron SAXS/WAXS measurements were performed at the 12-ID-B beamline of the Advanced Photon Source at Argonne National Laboratory. The sample-to-detector distances were set such that the overall scattering momentum transfer, q, range was achieved from 0.005 to 0.9 $Å^{-1}$, where $q = 4\pi \sin\theta/\lambda$, with 2θ denoting the scattering angle and λ denoting the X-ray wavelength. The wavelength was set at 0.9322 Å during the measurements. Scattered X-ray intensities were measured using a Pilatus 2 M (DECTRIS Ltd.) detector. Measurements were conducted on aqueous solutions of CMP nanosheets at a concentration of ∼2.5 mg/mL for $\mathbf{4R(X)}_{444}$@ $\mathbf{4S(X)}_{444}$ nanosheets and 4 mg/mL for $\mathbf{4R(X)}_{444}$ and $\mathbf{4S(X)}_{444}$ nanosheets in 20 mM MOPS buffer (pH 7.0) at 5 °C. A quartz capillary flow cell (1.5 mm diameter) was employed to prevent radiation damage. The 2D scattering images were converted to 1D scattering curves through azimuthal averaging after solid angle correction and then normalizing with the intensity of the transmitted X-ray beam using the software package at beamline 12-ID-B. The 1D curves of the samples were averaged and subtracted with the background measured from the corresponding buffers.

Cryogenic Transmission Electron Microscopy. The nanosheet sample was shipped and stored at 4 °C. Thereafter, it was briefly centrifuged to obtain a denser solution. Then 2 to 3 μL of the suspension was pipetted onto a glow-discharged QuantiFoil grid 1.2/1.3 (300 mesh). Grids were blotted for 3 s with blot force 1 and plunge-frozen in liquid ethane using a Vitrobot with the environmental chamber set at 100% humidity and 4 °C. Data were acquired on a Titan Krios electron microscope at 300 keV (Thermo Fisher) in nanoprobe mode, with a GIF Quantum LS Imaging filter (20 eV slit width) and a K2 Summit electron counting direct detection camera (Gatan).

Data sets at zero tilt were collected at nominal magnifications of 105K and 130K, resulting in calibrated physical pixel sizes of 1.336 and 1.056 Å, respectively. The defocus was set in the range of 0.1−0.5 μm. The data were collected with a modified in-house script using SerialEM.[39] Every position was selected manually by the observation of crystal-like features, and each of these positions was exposed by recording a 14.4−16.8 s movie with 36−56 frames totaling 50 $e^-/Å^2$.

The Focus software package[40] was used to drift correct the images with Motioncor2.[41] CTF correction was done with Gctf.[42] On the basis of FFTs of collected frames, a selection was made between single sheets and core−shell sheets. The unit cell of the $\mathbf{4R(X)}_{444}$@$\mathbf{4S(X)}_{444}$ nanosheets was confirmed for several images by measuring the distances of the lattice in the local Fourier transformations and in the real space. The images were filtered on the basis of a Wiener filter approach, which enhances lattice features without knowledge or input of the lattice parameters while assuming that the signal is uncorrelated to the noise.[43] These filtered images were analyzed and eventually used as an overlay on the original drift-corrected images.[44−46] Using the filtered information as an overlay, it was possible to identify locations of interest (i.e., lattice defects and distortions) over the whole crystal.

Fluorescence Optical Microscopy. The Nikon Eclipse Ti microscope was equipped with an Intensilight epifluorescence source (Nikon), a CFI Apo 100 × NA 1.49 objective (Nikon), and a TIRF launcher with three laser lines: 488 nm (10 mW), 561 nm (50 mW), and 638 nm (20 mW). All of the reported experiments were performed using the Quad Cube (cat. no. 97327) and TRITC (96321) filter cube set supplied by Chroma.

Experiments were conducted using no. 1.5 glass slides (25 × 75 mm) that were cleaned by sonication in Milli-Q (18.2 MΩ/cm) water for 15 min, followed by a second sonication in 200 proof ethanol for 15 min, and then dried under a stream of N_2. The slides were etched with piranha solution (v/v = 3:7 hydrogen peroxide/sulfuric acid) for 30 min to remove residual organic material and activate hydroxyl groups on the surface. The cleaned substrates were rinsed with Milli-Q water in a 200 mL beaker at least six times and further washed with ethanol three times. Slides were then transferred to a 200 mL beaker containing 2% (3-aminopropyl)triethoxysilane (APTES) in ethanol for 1 h and then washed with ethanol three times and thermally cured in an oven (∼110 °C) for 10 min. The APTES-functionalized slides were mounted to a custom-made 30-well microfluidic chamber fabricated from Delrin. The nanosheet solutions were added (10 μL) to the wells and were immediately subjected to a wash (3 × 100 μL) with 20 mM MOPS buffer (pH 7.0).

■ ASSOCIATED CONTENT

Supporting Information

The Supporting Information is available free of charge at https://pubs.acs.org/doi/10.1021/jacs.9b09335.

MALDI-TOF MS, HPLC, TEM, AFM, CD, and cryo-TEM data (PDF)

■ AUTHOR INFORMATION

Corresponding Author

*vcontic@emory.edu

ORCID

Andrea D. Merg: 0000-0002-2293-5267
Khalid Salaita: 0000-0003-4138-3477
Vincent P. Conticello: 0000-0001-6940-6947

Notes

The authors declare no competing financial interest.

■ ACKNOWLEDGMENTS

This work was supported by the NSF (CHE-1808509, V.P.C.) and used resources of the Advanced Photon Source, a U.S. Department of Energy (DOE) Office of Science User Facility operated for the DOE Office of Science by Argonne National Laboratory under contract no. DE-AC02-06CH11357. We thank Prof. Tianquan Lian and Prof. Brian Dyer for the use of the atomic force microscope and DLS instrument, respectively. We also acknowledge the following people: Lubomir Kovacik

DOI: 10.1021/jacs.9b09335
J. Am. Chem. Soc. 2019, 141, 20107−20117

and Henning Stahlberg for their help with microscope operation and the use of the cryo-TEM facility, respectively.

REFERENCES

(1) Govindaraju, T.; Avinash, M. B. Two-dimensional nanoarchitectonics: organic and hybrid materials. *Nanoscale* **2012**, *4* (20), 6102−6117.
(2) Ariga, K.; Ji, Q.; Hill, J. P.; Bando, Y.; Aono, M. Forming nanomaterials as layered functional structures toward materials nanoarchitectonics. *NPG Asia Mater.* **2012**, *4* (5), No. e17.
(3) Ariga, K.; Ji, Q.; Nakanishi, W.; Hill, J. P.; Aono, M. Nanoarchitectonics: a new materials horizon for nanotechnology. *Mater. Horiz.* **2015**, *2* (4), 406−413.
(4) Boott, C. E.; Nazemi, A.; Manners, I. Synthetic Covalent and Non-Covalent 2D Materials. *Angew. Chem., Int. Ed.* **2015**, *54* (47), 13876−13894.
(5) Zhuang, X.; Mai, Y.; Wu, D.; Zhang, F.; Feng, X. Two-Dimensional Soft Nanomaterials: A Fascinating World of Materials. *Adv. Mater.* **2015**, *27* (3), 403−427.
(6) Colson, J. W.; Dichtel, W. R. Rationally synthesized two-dimensional polymers. *Nat. Chem.* **2013**, *5*, 453.
(7) Zhang, H. Ultrathin Two-Dimensional Nanomaterials. *ACS Nano* **2015**, *9* (10), 9451−9469.
(8) Ariga, K.; Watanabe, S.; Mori, T.; Takeya, J. Soft 2D nanoarchitectonics. *NPG Asia Mater.* **2018**, *10* (4), 90−106.
(9) Zhang, S.; Zhang, J.; Fang, W.; Zhang, Y.; Wang, Q.; Jin, J. Ultralarge Single-Layer Porous Protein Nanosheet for Precise Nanosize Separation. *Nano Lett.* **2018**, *18* (10), 6563−6569.
(10) Zhang, X.; Xie, Y. Recent advances in free-standing two-dimensional crystals with atomic thickness: design, assembly and transfer strategies. *Chem. Soc. Rev.* **2013**, *42* (21), 8187−8199.
(11) Sakamoto, J.; van Heijst, J.; Lukin, O.; Schlüter, A. D. Two-Dimensional Polymers: Just a Dream of Synthetic Chemists? *Angew. Chem., Int. Ed.* **2009**, *48* (6), 1030−1069.
(12) Jin, H.; Guo, C.; Liu, X.; Liu, J.; Vasileff, A.; Jiao, Y.; Zheng, Y.; Qiao, S.-Z. Emerging Two-Dimensional Nanomaterials for Electrocatalysis. *Chem. Rev.* **2018**, *118* (13), 6337−6408.
(13) Palma, C.-A.; Samorì, P. Blueprinting macromolecular electronics. *Nat. Chem.* **2011**, *3*, 431.
(14) Jia, X.; Minami, K.; Uto, K.; Chang, A. C.; Hill, J. P.; Ueki, T.; Nakanishi, J.; Ariga, K. Modulation of Mesenchymal Stem Cells Mechanosensing at Fluid Interfaces by Tailored Self-Assembled Protein Monolayers. *Small* **2019**, *15* (5), 1804640.
(15) He, X.; Hsiao, M.-S.; Boott, C. E.; Harniman, R. L.; Nazemi, A.; Li, X.; Winnik, M. A.; Manners, I. Two-dimensional assemblies from crystallizable homopolymers with charged termini. *Nat. Mater.* **2017**, *16*, 481.
(16) Nazemi, A.; He, X.; MacFarlane, L. R.; Harniman, R. L.; Hsiao, M.-S.; Winnik, M. A.; Faul, C. F. J.; Manners, I. Uniform "Patchy" Platelets by Seeded Heteroepitaxial Growth of Crystallizable Polymer Blends in Two Dimensions. *J. Am. Chem. Soc.* **2017**, *139* (12), 4409−4417.
(17) Yu, B.; Jiang, X.; Yin, J. Size-Tunable Nanosheets by the Crystallization-Driven 2D Self-Assembly of Hyperbranched Poly(ether amine) (hPEA). *Macromolecules* **2014**, *47* (14), 4761−4768.
(18) He, X.; He, Y.; Hsiao, M.-S.; Harniman, R. L.; Pearce, S.; Winnik, M. A.; Manners, I. Complex and Hierarchical 2D Assemblies via Crystallization-Driven Self-Assembly of Poly(l-lactide) Homopolymers with Charged Termini. *J. Am. Chem. Soc.* **2017**, *139* (27), 9221−9228.
(19) Evans, A. M.; Parent, L. R.; Flanders, N. C.; Bisbey, R. P.; Vitaku, E.; Kirschner, M. S.; Schaller, R. D.; Chen, L. X.; Gianneschi, N. C.; Dichtel, W. R. Seeded growth of single-crystal two-dimensional covalent organic frameworks. *Science* **2018**, *361* (6397), 52−57.
(20) Qiu, H.; Gao, Y.; Boott, C. E.; Gould, O. E. C.; Harniman, R. L.; Miles, M. J.; Webb, S. E. D.; Winnik, M. A.; Manners, I. Uniform patchy and hollow rectangular platelet micelles from crystallizable polymer blends. *Science* **2016**, *352* (6286), 697.
(21) Hudson, Z. M.; Boott, C. E.; Robinson, M. E.; Rupar, P. A.; Winnik, M. A.; Manners, I. Tailored hierarchical micelle architectures using living crystallization-driven self-assembly in two dimensions. *Nat. Chem.* **2014**, *6*, 893.
(22) Jiang, T.; Xu, C.; Liu, Y.; Liu, Z.; Wall, J. S.; Zuo, X.; Lian, T.; Salaita, K.; Ni, C.; Pochan, D.; Conticello, V. P. Structurally Defined Nanoscale Sheets from Self-Assembly of Collagen-Mimetic Peptides. *J. Am. Chem. Soc.* **2014**, *136* (11), 4300−4308.
(23) Jiang, T.; Xu, C.; Zuo, X.; Conticello, V. P. Structurally Homogeneous Nanosheets from Self-Assembly of a Collagen-Mimetic Peptide. *Angew. Chem., Int. Ed.* **2014**, *53* (32), 8367−8371.
(24) Merg, A. D.; Touponse, G.; van Genderen, E.; Zuo, X.; Bazrafshan, A.; Blum, T.; Hughes, S.; Salaita, K.; Abrahams, J. P.; Conticello, V. P. 2D Crystal Engineering of Nanosheets Assembled from Helical Peptide Building Blocks. *Angew. Chem., Int. Ed.* **2019**, *58* (38), 13507−13512.
(25) Egli, J.; Siebler, C.; Maryasin, B.; Erdmann, R. S.; Bergande, C.; Ochsenfeld, C.; Wennemers, H. pH-Responsive Aminoproline-Containing Collagen Triple Helices. *Chem. - Eur. J.* **2017**, *23* (33), 7938−7944.
(26) Park, S. H.; Yin, P.; Liu, Y.; Reif, J. H.; LaBean, T. H.; Yan, H. Programmable DNA Self-Assemblies for Nanoscale Organization of Ligands and Proteins. *Nano Lett.* **2005**, *5* (4), 729−733.
(27) Wittmann, J. C.; Lotz, B. Epitaxial crystallization of polyethylene on organic substrates: A reappraisal of the mode of action of selected nucleating agents. *J. Polym. Sci., Polym. Phys. Ed.* **1981**, *19* (12), 1837−1851.
(28) Williams, D. B.; Carter, C. B. *Transmission Electron Microscopy: A Textbook for Materials Science*, 2nd ed.; Springer: New York, 2009; p 775.
(29) Palmstrom, C. J. Epitaxy of Dissimilar Materials. *Annu. Rev. Mater. Sci.* **1995**, *25* (1), 389−415.
(30) Ohring, M. *Materials Science of Thin Films: Deposition and Structure*, 2nd ed.; Academic Press: San Diego, 2002; Chapter 8, pp 417−494.
(31) Gabrys, P. A.; Seo, S. E.; Wang, M. X.; Oh, E.; Macfarlane, R. J.; Mirkin, C. A. Lattice Mismatch in Crystalline Nanoparticle Thin Films. *Nano Lett.* **2018**, *18* (1), 579−585.
(32) Persikov, A. V.; Ramshaw, J. A. M.; Brodsky, B. Prediction of Collagen Stability from Amino Acid Sequence. *J. Biol. Chem.* **2005**, *280* (19), 19343−19349.
(33) Okuyama, K. Revisiting the Molecular Structure of Collagen. *Connect. Tissue Res.* **2008**, *49* (5), 299−310.
(34) Okuyama, K.; Xu, X.; Iguchi, M.; Noguchi, K. Revision of collagen molecular structure. *Biopolymers* **2006**, *84* (2), 181−191.
(35) Jiang, T.; Vail, O. A.; Jiang, Z.; Zuo, X.; Conticello, V. P. Rational Design of Multilayer Collagen Nanosheets with Compositional and Structural Control. *J. Am. Chem. Soc.* **2015**, *137* (24), 7793−7802.
(36) Qian, J.; Guerin, G.; Lu, Y.; Cambridge, G.; Manners, I.; Winnik, M. A. Self-Seeding in One Dimension: An Approach To Control the Length of Fiberlike Polyisoprene−Polyferrocenylsilane Block Copolymer Micelles. *Angew. Chem., Int. Ed.* **2011**, *50* (7), 1622−1625.
(37) Gilroy, J. B.; Gädt, T.; Whittell, G. R.; Chabanne, L.; Mitchels, J. M.; Richardson, R. M.; Winnik, M. A.; Manners, I. Monodisperse cylindrical micelles by crystallization-driven living self-assembly. *Nat. Chem.* **2010**, *2*, 566.
(38) Moving towards the market. *Nat. Mater.* **2019**, *18*(6), 519−519.
(39) Mastronarde, D. N. Automated electron microscope tomography using robust prediction of specimen movements. *J. Struct. Biol.* **2005**, *152* (1), 36−51.
(40) Biyani, N.; Righetto, R. D.; McLeod, R.; Caujolle-Bert, D.; Castano-Diez, D.; Goldie, K. N.; Stahlberg, H. Focus: The interface between data collection and data processing in cryo-EM. *J. Struct. Biol.* **2017**, *198* (2), 124−133.
(41) Li, X.; Mooney, P.; Zheng, S.; Booth, C. R.; Braunfeld, M. B.; Gubbens, S.; Agard, D. A.; Cheng, Y. Electron counting and beam-

DOI: 10.1021/jacs.9b09335
J. Am. Chem. Soc. 2019, 141, 20107−20117

induced motion correction enable near-atomic-resolution single-particle cryo-EM. *Nat. Methods* **2013**, *10*, 584.
(42) Zhang, K. Gctf: Real-time CTF determination and correction. *J. Struct. Biol.* **2016**, *193* (1), 1−12.
(43) van Genderen, E.; Li, Y.-W.; Nederlof, I.; Abrahams, J. P. Lattice filter for processing image data of three-dimensional protein nanocrystals. *Acta Crystallogr. D* **2016**, *72* (1), 34−39.
(44) Schindelin, J.; Arganda-Carreras, I.; Frise, E.; Kaynig, V.; Longair, M.; Pietzsch, T.; Preibisch, S.; Rueden, C.; Saalfeld, S.; Schmid, B.; Tinevez, J.-Y.; White, D. J.; Hartenstein, V.; Eliceiri, K.; Tomancak, P.; Cardona, A. Fiji: an open-source platform for biological-image analysis. *Nat. Methods* **2012**, *9*, 676.
(45) Schindelin, J.; Rueden, C. T.; Hiner, M. C.; Eliceiri, K. W. The ImageJ ecosystem: An open platform for biomedical image analysis. *Mol. Reprod. Dev.* **2015**, *82* (7−8), 518−529.
(46) Schneider, C. A.; Rasband, W. S.; Eliceiri, K. W. NIH Image to ImageJ: 25 years of image analysis. *Nat. Methods* **2012**, *9*, 671.

DOI: 10.1021/jacs.9b09335
J. Am. Chem. Soc. 2019, 141, 20107−20117